

COMPASS: a new COnductance Model based on PFISR And SWARM Satellite observations

Zihan Wang¹, Shasha Zou¹

¹Department of Climate and Space Sciences and Engineering, University of Michigan, Ann Arbor, MI,
USA

Key Points:

- Ionospheric conductance varies as a power of $|j_{\parallel}|$.
- The power index peaks on the dawn side and dips at noon.
- Upward FACs are associated with larger power indices than downward FACs.

Corresponding author: Zihan Wang, wzihan@umich.edu

Abstract

Ionospheric conductance plays a crucial and active role in magnetosphere-ionosphere-thermosphere coupling processes. Despite its importance, direct global observations of conductance are unavailable. This limitation inspires the development of empirical models that are widely used to specify global distributions of conductance indirectly. In this work, a new model (COMPASS) describing the statistical relationships between conductance and Field-Aligned Currents (FACs) is presented. The conductance was determined by the electron densities measured by Poker Flat Incoherent Scattering Radar (PFISR), and the FACs were determined by the magnetic perturbations measured by SWARM. Between 2014 and 2020, there were ~ 3900 conjunction events between PFISR and SWARM, providing a large dataset for investigating the relationship between conductance and FACs. It is found that both Hall and Pedersen conductances vary as a power of $|j_{\parallel}|$, and the power index a is between 0 and 0.5. This power index a depends on the Magnetic Local Time (MLT) and the direction of FACs: (1) The largest power index is obtained on the dawn side, and the minimum is at noon, suggesting the strongest/weakest correlation in the dawn/noon sector; (2) the power indices are positive for both upward and downward FACs and are larger for upward FACs than downward FACs, except in the dusk sector. The underlying physical mechanisms of the observed variations of the model parameters are also discussed. This work sheds light on the complicated relationship between FACs and conductance and provides a convenient way to specify global distributions of the auroral zone conductance.

Plain Language Summary

Ionospheric conductance is a crucial parameter in the modeling of the geospace response to varying solar wind forcing. However, direct global observations of conductance are unavailable. This limitation inspires the development of this new model (COMPASS) describing the statistical relationships between conductance and Field-Aligned Currents (FACs). Global distributions of FACs are easy to obtain from either observations or numerical simulations. Thus, this model provides a convenient way to specify the global distribution of the ionospheric conductance.

1 Introduction

Ionospheric height-integrated conductivity (conductance) is a key parameter in the dynamic coupling processes among the magnetosphere, the ionosphere, and the thermosphere. It is mainly produced by photoionization on the dayside due to solar radiation and can be altered by auroral precipitation from the magnetosphere and solar wind due to impact ionization. Variations in conductance can in turn influence magnetospheric convection. The increase of conductance can also lead to an expansion of the thermosphere through Joule Heating, which subsequently modifies the conductance. Because of the importance of conductance in the coupled system, it is necessary to better determine its distribution to improve the characterization of high-latitude electrodynamics.

A number of approaches have been utilized to specify the high-latitude conductance. One conventional direct method is to measure the altitude profiles of electron density in the ionosphere using Incoherent Scattering Radars (ISRs). Then, the density profiles are used to calculate conductivity. However, due to the limited spatial coverage of ISRs, it is impossible to obtain a global map of conductance. An indirect method is to measure auroral precipitation (e.g., energy flux and average energy) and then estimate the conductance (e.g. Coumans et al., 2004; Fuller-Rowell & Evans, 1987; Germany et al., 1994; Hardy et al., 1987; Lummerzheim et al., 1991; McGranaghan et al., 2015; Spiro et al., 1982; Wallis & Budzinski, 1981). Precipitation can be measured in-situ by spectrometer onboard Low-Earth Orbital (LEO) satellites (e.g. Fuller-Rowell & Evans, 1987; Hardy et al., 1987; McGranaghan et al., 2015; Spiro et al., 1982; Wallis & Budzinski, 1981).

or inferred from the optical emissions observed by auroral imagers onboard satellites (e.g. Lummerzheim et al., 1991; Germany et al., 1994; Coumans et al., 2004). Observed precipitation information is then passed into empirical (e.g. Robinson et al., 1987) or numerical models (e.g. Solomon et al., 1988) to obtain electron density profiles and/or conductance. However, the precipitation observed by in-situ spectrometers cannot provide a global coverage, and the precipitation inferred from imagers onboard satellites may not provide data with sufficient temporal cadence. Besides satellite observations, precipitation can also be inferred from ground-based measurements. For instance, Kaeppler et al. (2015) combined the observations from All Sky Imagers and scanning Doppler Imaging Fabry-Perot interferometers to calculate conductance. Grubbs II et al. (2018) also reported that the multispectral images can be used to estimate the characteristics of precipitating in the inverted-V aurora. However, these techniques cannot provide a global coverage either.

Due to the limitations of observations, numerous empirical models were developed to specify conductance distributions in the absence of direct observation assets. A group of empirical models depend on solar wind or geomagnetic conditions (e.g. Carter et al., 2020; Fuller-Rowell & Evans, 1987; Hardy et al., 1987; Spiro et al., 1982; Wallis & Budzinski, 1981). Due to their statistical nature, these empirical models provide smooth conductance distributions without meso-scale spatial structures that are necessary for accurate ionospheric electrodynamic specification (Robinson et al., 2020). Conductance can also be expressed as a function of ground magnetic disturbances (Ahn et al., 1983, 1998) or FACs (Ridley et al., 2004; Mukhopadhyay et al., 2020). Unlike the models that depend on solar wind and/or geomagnetic conditions, the dependence on these two types of local observations enables capturing the spatial and temporal details of conductance. Furthermore, a global coverage and a high time cadence of both types of observations are available (Anderson et al., 2014; Gjerloev, 2012), meaning that a continuous global map of conductance is achievable. Recently, Robinson et al. (2020) reported a linear relationship between FACs and conductance in both upward and downward current regions over some MLTs based on AMPERE and PFISR observations. Robinson et al. further built a framework to characterize various electrodynamics variables (e.g., electric fields, Joule heating rate) in the high-latitude region based on AMPERE data (Robinson et al., 2018, 2020, 2021; Robinson & Zanetti, 2021).

Launched in 2013, SWARM has high-precision magnetometers measuring the magnitude and direction of the magnetic field, and thus the FACs can be derived from the calculated magnetic perturbation with high spatial and temporal resolution (Lühr et al., 2016), but no global coverage. Thus, we aim to build a conductance model using FACs data from SWARM and conductance data from PFISR, which can later be used to specify global conductance based on FACs from AMPERE observations or numerical simulations. It is also interesting to investigate whether different FAC data sources can lead to a different relationship between FACs and conductance.

The purpose of this work is to investigate the statistical relationship between FACs and conductance using a combination of SWARM and PFISR observations. The plan of this paper is as follows. In Section 2, the datasets used in this study are introduced. In Section 3, the statistical relationship between FACs and conductance is analyzed based on the observations in darkness; the new model is further tested on the observations in sunlight. In Section 4, physical implications, limitations, and applications of the relationship are discussed.

2 Methods

In this work, conductance was calculated based on the electron density measurements from PFISR (Heinselman & Nicolls, 2008), which is located at $65.13^{\circ}N$, $147.47^{\circ}W$ in Alaska. PFISR can offer subauroral or auroral zone observations depending on geo-

magnetic activity levels. Operating in alternating coded (AC) pulses, it provides altitude density profiles with an altitude resolution of ~ 4.5 km. These profiles were then used to calculate conductance. The formulas for calculating the Pedersen and Hall conductivities are given by

$$\sigma_P(z) = \frac{en(z)}{B(z)} \left[\frac{\nu_{en}\Omega_e}{\nu_{en}^2 + \Omega_e^2} + \sum_i C_i \frac{\nu_{in}\Omega_i}{\nu_{in}^2 + \Omega_i^2} \right], \quad (1)$$

$$\sigma_H(z) = \frac{en(z)}{B(z)} \left[\frac{\Omega_e^2}{\nu_{en}^2 + \Omega_e^2} - \sum_i C_i \frac{\Omega_i^2}{\nu_{in}^2 + \Omega_i^2} \right], \quad (2)$$

where $n(z)$ is the electron density measured by ISR, Ω is the gyro frequency, C_i is the number abundance of different ions, ν_{en} is the collision frequency between electrons and neutrals, and ν_{in} is the collision frequency between ions and neutrals. i represents the different species of ions. In this study, important major ion and neutral species O^+ , O_2^+ , NO^+ , N_2 , O_2 and O were considered. The collision coefficients were taken from Schunk and Nagy (2009), the neutral densities were from MSIS (Picone et al., 2002), and the local magnetic fields were from International Geomagnetic Reference Field (IGRF) (Thébault et al., 2015). In this work, only data from the field-aligned beam was used, along which the calculated conductivity was integrated to obtain conductance.

FACs were derived from the magnetic field perturbation measurements from the SWARM mission (Ritter et al., 2013). SWARM consists of three identical satellites in a near-polar (87.5° inclination) orbit. SWARM-A and -C, are flying side by side, separated by only 1.4° in longitude and at an altitude of about 460 km, while SWARM-B orbits the Earth at about 520 km with a higher inclination. Based on the magnetic field measurements of a single satellite, FACs can be derived with the assumption that the FAC current sheets are perpendicular to the flight directions. Lühr et al. (2014) suggested that FACs with latitudinal scales less than 150 km cannot be determined reliably from single-satellite measurements. Therefore, in this study, FAC variations were smoothed with a moving average window of 21 s (a latitudinal scale of 150 km). Note that an alternative method, a low-pass filter with a cutoff frequency of 0.05 Hz, has also been used to remove the high frequency fluctuation of the FACs. The filtered FACs were then used to identify the relationship between FACs and conductance. The results show that the relationship between FACs and conductance is not sensitive to the filters used. Thus, in this paper, we present the FACs after the moving average. SWARM also offers a FAC database using a dual-satellite technique (SWARM- A and C). However, this database is much smaller. To make sure a sufficiently large FAC dataset for statistical analysis, we chose to use the single-satellite FAC instead of the dual-satellite.

To determine the conjunction between the SWARM satellites and PFISR, the location of PFISR was first mapped to the altitude of SWARM using Altitude-Adjusted Corrected Geomagnetic (AACGM) (Shepherd, 2014). The mapped location was then compared to the location of the satellite. The comparison criteria were as follows: the longitudinal difference between the satellite and PFISR should be less than 4 degrees. This specific number was chosen because the longitudinal scale of FACs with a latitudinal scale of 150 km was about 4 degrees on the nightside (Lühr et al., 2014). During each orbit, the time cadence when the satellite was closest to PFISR in latitude was selected, i.e., the latitudinal difference between the SWARM satellite and PFISR was less than 0.075 degrees (7.5 km). In total, there were ~ 3900 available conjunction events between 2014 and 2020. These events had simultaneous FAC and conductance measurements.

The distributions of conjunction events as a function of MLT, Dst, F10.7, and months are shown in Figure 1. Several trends can be found in this dataset: (1) there is an even distribution across different MLTs. (2) A majority of the cases occur during quiet or moderate geomagnetic activity with Dst larger than -50 nT, similar to the general Dst distribution. (3) A majority of the cases occur during or near the solar minimum of solar

cycle 24 with F10.7 smaller than 100 sfu. (4) The event distribution as a function of month is roughly uniform, except November.

All cases were then divided into two subsets: in darkness (A) and in sunlight (B). If the solar zenith angle (SZA) was larger than 90 degrees, then the case was in Dataset A (in darkness). Otherwise, it was in Dataset B (in sunlight). The relationship between FACs and conductance was investigated solely in Dataset A to avoid contributions from solar radiation-induced photoionization. Another reason is that FACs are more sheet-like on the nightside than on the dayside (Lühr et al., 2014), i.e., the FACs based on a single satellite are more reliable on the nightside. The newly derived empirical model was later tested on Dataset B.

3 Data Analysis

3.1 New Parameters Obtained using Dataset A

Figure 2 shows the scatter plots of FACs vs conductance in Dataset A in a log-log scale. A linear relationship between $\ln(|j_{\parallel}|)$ and $\ln(\Sigma)$ exists despite strong scatter. The scatter decreases as the amplitude of FACs increases, in particular in the upward FAC case. To better capture the statistical trend, all data points were binned into 3-hour MLT intervals before linear least square fitting was conducted. Fitting results are shown in Figures 3-6 and Table 1. Note that the cases between 9 and 12 MLT are so few that the fitting is not applicable. According to the linear least square fitting between $\ln(|j_{\parallel}|)$ and $\ln(\Sigma)$, the Pedersen and Hall conductances are given as

$$\ln(\Sigma_{P \text{ or } H}) = k \times \ln(|j_{\parallel}|) + b, \quad (3)$$

It can also be written as

$$\Sigma_{P \text{ or } H} = c \times |j_{\parallel}|^a, \quad (4)$$

where $k = a$ and $c = e^b$. All parameters (k, b, c, a) depend on both the MLT and the direction of FACs. The results show that the power index is much less than 1, different from the linear relationship in Robinson et al. (2020). In addition, the slopes are all positive except in two bins: upward vs Pedersen between 12 and 15 MLT, and downward vs Pedersen between 6 and 9 MLT. Both of them have near zero slopes although slightly negative. Furthermore, it is worthwhile to note that the slopes for both upward and downward FACs are larger on the nightside (MLT > 18 or MLT < 6), suggesting a stronger dependence of the conductance on the FAC magnitude on the nightside.

Figures 7 and 8 further shows the dependence of the fitting parameters on MLTs. The error bars represent the one-sigma uncertainties of the slopes and intercepts. When the model is applied, the negative parameters are regarded as zero to avoid the infinitely large conductance when FACs are close to zero. In addition, the slopes and intercepts between 9 and 12 MLT are calculated using linear interpolation and thus have no error bars. The slopes peak in the 3-6 MLT sector and dip in the noon sector for all four relationships. On the dawn side, the slopes of upward FACs are significantly larger than those of downward FACs. However, on the dusk side, the difference is much smaller. Between 15 and 18 MLT, the slopes of downward FACs are even larger than those of upward FACs. In addition, the slopes of Hall conductance are larger than those of the Pedersen conductance on the dawn side, while the difference again minimizes on the dusk side. Similar features are also found in the intercepts plot. The physical implications of these results are discussed later in Section 4. In the next section, this new empirical model is tested using Dataset B.

3.2 Testing New Parameters using Dataset B

All events in Dataset B are in the sunlit region, so the conductance was calculated by including solar photoionization

$$\Sigma_P = (\Sigma_{P_{solar}}^2 + \Sigma_{P_{prec}}^2)^{1/2}, \quad (5)$$

$$\Sigma_H = (\Sigma_{H_{solar}}^2 + \Sigma_{H_{prec}}^2)^{1/2}. \quad (6)$$

Because the ionization rates at each altitude add linearly (Robinson et al., 2020), and the ionization rate is proportional to the square of the electron density and conductance, a quadratic summation is often used. According to Moen and Brekke (1993), the solar radiation-induced conductance contribution is empirically given by

$$\Sigma_{P_{solar}} = F_{10.7}^{0.49} (0.34 \cos(SZA) + 0.93 \cos^{0.5}(SZA)), \quad (7)$$

$$\Sigma_{H_{solar}} = F_{10.7}^{0.53} (0.81 \cos(SZA) + 0.54 \cos^{0.5}(SZA)). \quad (8)$$

where the F10.7 parameter is the solar radio flux measured at 10.7 cm with a unit of solar flux unit (sfu), and SZA is the solar zenith angle. The conductance due to precipitating particle impact ionization was calculated using the new empirical model. After the quadratic summation, the total estimated conductance was compared with the observed value. The comparisons are shown in Figure 9. In these comparisons, three metrics were used to evaluate the performance of the model: Root Mean Square Error (RMSE), Prediction Efficiency (PE), and Mean Error (ME). The definition of each metric is as follows:

$$RMSE = \sqrt{\frac{1}{N-d} \sum_{i=1}^N (M_i - O_i)^2}, \quad (9)$$

$$PE = 1 - \frac{\sum (M_i - O_i)^2}{\sum (O_i - \bar{O})^2}, \quad (10)$$

$$ME = \bar{M} - \bar{O}, \quad (11)$$

where N represents total data points, d is the degrees of freedom, M_i represents the estimations, and O_i represents the observations. In this model, d is 3 (j_{\parallel} , $F_{10.7}$, and SZA). RMSE represents the accuracy of the model with a unit of mho. PE represents the fitting performance skill score, also known as the coefficient of determination. An ideal PE is 1, meaning that the model can fit the observations perfectly. A value of PE less than zero means that the model is worse than the average of the data at predicting the observations. ME represents the bias of the model with a unit of mho.

As shown in Figures 9a and 9c, the absolute values of MEs of Pedersen conductance for both upward and downward FACs cases are smaller than 0.2 mho. This means that the model predicts Pedersen conductance accurately on average. In Figures 9b and 9d, the MEs are negative and around 1 mho, suggesting that the model might slightly underestimate the Hall conductance. In all panels, PEs are larger than zero, meaning that the model can provide meaningful predictions. The PEs of the upward FACs (Figures 9a-9b) are larger than those of downward FACs (Figures 9c-9d), showing the model can predict the conductance under upward FACs more accurately.

The RMSEs and PEs of this model were further compared with those in Robinson et al. (2020) to test its performance. In this comparison, both datasets (A and B) were

used. As shown in Figure 10, the RMSE of the Pedersen conductance is 3.17 mho, and the RMSE of Hall conductance is 7.23 mho. Both are comparable but smaller than the RMSEs in Robinson et al. (2020) (Pedersen: 3.75 mho; Hall: 9.12 mho). In our model, the PE of the Pedersen/Hall conductance is 0.37/0.33. In their model, the PE scores of Pedersen and Hall conductance are 0.18 and 0.30, respectively. The above results demonstrate that the new empirical model can provide good estimates of conductance, and our model showed a comparable but slightly better performance.

4 Discussions

In this section, the underlying physical implications, as well as limitations and potential applications of this new empirical model are discussed.

4.1 Power Law Dependence

Figures 3-6 show that conductance varies as a power of $|j_{\parallel}|$, and the power indices for different MLTs are between 0 and 0.5. Conductance has been shown to vary as a power of the precipitation energy flux for both protons and electrons, and the power index is around 0.5 (Galand & Richmond, 2001; Germany et al., 1994; Robinson et al., 1987). Korth et al. (2014) reported that the electron energy flux was proportional to the square of FACs in the afternoon. Therefore, in this case, the conductance should change almost linearly with the magnitude of FACs, i.e., a power index around 1 in the afternoon, as Robinson et al. (2020) suggested. However, at other MLTs, upward FACs and electron energy fluxes are not well correlated (Korth et al., 2014), suggesting that even the relationship between upward FACs and precipitation is complicated. For example, ion outflow may need to be considered as additional current carriers (Xiong et al., 2020). Thus, it is not surprising that the conductance can be expressed as a power of FACs, but the power index differs from 1. In addition, it is found that the conductance varies as a power of the ground magnetic perturbations in the north-south direction (Ahn et al., 1983). In that study, the power index is also between 0 and 1. The similarity of the magnitude of the power index between our work and the work by Ahn et al. (1983) implies a close relationship between FACs and ground magnetic perturbations in the north-south direction (Weygand et al., 2011), consistent with our conventional current closure picture in the auroral zone (Kamide, 1982).

Figures 3-6 also show that both upward and downward FACs are positively correlated with conductance in most MLTs except near the morning sector. It is generally agreed that upward FACs are closely related to discrete aurora and energetic electron precipitation (e.g. Knight, 1973; Korth et al., 2014). However, the positive correlation relationship between downward FACs and particle precipitation is less reported. Robinson et al. (2020) also found a linear positive relationship between the magnitude of downward FACs and conductance. The increase of conductance under downward FACs can be partly explained by the background electron diffuse precipitation and/or proton precipitation: downward FACs may occur in regions of electron diffuse aurora during substorms (Murphy et al., 2013); downward FACs can be carried by precipitating protons (Xiong et al., 2020). Carter et al. (2016) further showed that the region 2 (downward) FACs were more closely aligned with the peak of proton aurora emission at dusk. In addition, Zou et al. (2009) reported precipitating proton-induced ionization in the dusk sector associated with Subauroral Polarization Streams (SAPS) in the Region-2 downward FAC region. These observations are consistent with the positive relationship found between the downward FACs and conductance.

4.2 MLT variations of power index

Figures 7-8 show that both the slopes and the intercepts of the FAC-conductance fitting are larger on the nightside. The maximum of these fitting parameters is located between 3 and 6 MLT, while their minimum is around noon. This local time dependence can be understood by invoking the MLT dependence of precipitating electrons. The average electron energy and the electron energy flux on the dayside are much lower than the nightside (Newell et al., 2009). These precipitating electrons cannot penetrate deep in the upper atmosphere and thus cannot contribute significantly to the conductance (Robinson et al., 2020). However, a large number of these low energy electrons can carry a significant amount of currents. In addition, the electron energy flux peaks on the night side (Newell et al., 2009), generating larger conductance, while both upward and downward FACs typically peak on the day side (He et al., 2012; Iijima & Potemra, 1978). As a result, a stronger relationship or a larger slope between the FACs and conductance is needed to account for the larger conductance on the night side, as shown in our results.

On the night side, it is shown that the slopes in the postmidnight sector are larger than those in the premidnight sector. This can also be explained by the larger energy flux on the dawn side. Xiong et al. (2020) showed that the electron energy flux is larger at dawn than that at dusk, even though the magnitudes of the upward FACs were comparable. This also implies that the average energy of the precipitating electrons is higher at dawn than that at dusk (Newell et al., 2010), thus generating larger conductance (Robinson et al., 1987).

On the dawn side, the four lines representing the slopes in Figure 7 are widely spaced from each other. The order of the slope magnitude is as follows: Upward vs Hall > Upward vs Pedersen > Downward vs Hall > Downward vs Pedersen. This order can be easily understood as follows. Upward FACs are usually associated with stronger electron precipitation flux and larger average energy, generating larger conductance; energetic precipitating electrons can penetrate deeper into the atmosphere, and thus the induced Hall conductance is usually larger than the Pedersen conductance. However, between 15 and 18 MLT, the order of the slope magnitude is inverted: Upward vs Hall < Upward vs Pedersen < Downward vs Hall < Downward vs Pedersen. On the dusk side, the slopes for the Hall conductance are lower than those for the Pedersen conductance for the same FAC polarity. This can either be explained by the fact that the average energy of precipitating electrons is lower on the dusk side than that on the dawn side (Newell et al., 2010) or by the fact that the proton precipitations contribute more to the Pedersen conductance due to proton beam spreading and thus stopping at higher altitudes (Fang et al., 2013).

At the dusk side, the slopes associated with downward FACs are larger than those with upward FACs for both Petersen and Hall conductances. This puzzling signature may again be explained by invoking the proton precipitation on the dusk side. The more sensitive dependence of the conductance on the downward FACs in the dusk sector implies that these downward FACs are carried by precipitating protons. Carter et al. (2016) showed that at dusk the region 2 (downward) FACs collocate with the peak of proton aurora. This suggests that the downward FACs are accompanied by a strong proton flux as current carriers. If the energy flux is the same, the proton precipitation can generate a larger Pedersen conductance than the electron precipitation (Galand & Richmond, 2001). In addition, Hall conductance is more sensitive to electron average energy than proton average energy (Galand & Richmond, 2001). Considering the higher proton energy flux and the lower average energy of the electron precipitation on the dusk side, the proton precipitation may generate a larger conductance than the electron precipitation. Note that the slope and intercept values at 12-15 MLTs are clustered, and the uncertainties are too large for meaningful distinction.

4.3 Model performance

Figure 9 shows that the PE under upward FACs is larger than that under downward FACs. This is because the upward FACs are mainly carried by precipitating electrons, which are expected to increase the conductance via impact ionization (e.g. Knight, 1973; Korth et al., 2014). On the other hand, the relationship between the downward FACs and particle precipitation is more complicated. In the case of precipitating protons as downward FAC carriers, they can increase the conductance via impact ionization (Galand & Richmond, 2001). If the downward FACs are mainly carried by upward going ionospheric electrons, the conductance is expected to decrease as a result of reduced ionospheric density due to evacuation (Karlsson & Marklund, 1998; Karlsson et al., 2007; Zou et al., 2013). Therefore, due to the complex current carriers of downward FACs, it is not surprising that the model performs better under upward FACs.

The quantitative metrics in the previous section indicate that the model can provide reasonable estimations of the conductance. However, several limitations should be considered. First, there are few cases (2 %) with FACs larger than $1\mu A/m^2$, because the majority of the conjunction dataset is during the geomagnetic quiet or moderate activity time. In addition, the linear least square fitting in a log-log scale skews toward small values. These two factors may lead to an underestimation of conductance when the FACs are large. Caution is needed when applying the model to extreme events since extreme events are rarely observed in the dataset used to train this model. Second, FACs are indirectly associated with the conductance and these two parameters are linked by current carriers. Usually, the precipitating flux and average energy are used together to specify conductance (e.g. Robinson et al., 1987). Recently, the whole precipitating particle energy spectra have been used in the GLOW model to calculate conductance (McGranaghan et al., 2015). Adding more variables (e.g., average energy) may improve the performance by including more physics. However, accurate characteristics of global precipitation are hard to obtain in both observations and simulations. Single variable (i.e., FAC) is used in this work to ensure that the model is easy to apply. The last caveat is that the model is based on PFISR observations and thus needs to be further tested for other latitudes, such as the polar cap. Under different geomagnetic conditions, PFISR can be in the sub-auroral region or auroral oval, but rarely in the polar cap. Generalization of this model to other latitudes will be the focus of our future work.

4.4 Potential application

The primary goal of this model is to improve the estimation of the global ionospheric conductance distribution and apply these conductance maps to global MHD simulations, because an accurate description of the conductance is of vital importance to improve the performance of space weather modeling. Up till now, several models have been proposed with different functions between FACs and conductance: linear function (Robinson et al., 2020); exponential function (Ridley et al., 2004); power function (this work). It is useful to plug the different conductance models into a standard modeling framework, e.g., SWMF, and assess their performances, which is similar to the validation efforts in Pulkkinen et al. (2013), or perform ensemble runs to provide uncertainty quantification forecasts. In addition, the model could be further used to characterize various electrodynamic variables in the high-latitude region, such as the work performed in Robinson et al. (2018, 2020, 2021); Robinson and Zanetti (2021). Our model provides another option for the community to estimate the global conductance distribution using the FAC information either from measurements (e.g., AMPERE), from empirical models of FACs, or numerical models that can calculate FACs.

5 Summary and conclusions

Based on the conjunction observations from SWARM and PFISR between 2014 and 2020, a power-law relationship between the conductance and FACs is found: $\Sigma_{P \text{ or } H} = c|j_{\parallel}|^a$. The power index a is between 0 and 0.5. We show that both Hall and Pedersen conductances increase with the magnitudes of both upward and downward FACs. In addition, upward FACs are associated with a larger power index than downward FACs, suggesting a stronger dependence of conductance on upward FACs. The power index varies as a function of MLTs. The largest power or the strongest dependence of conductance on FACs is found in the postmidnight sector, and the smallest power index or the weakest dependence is around noon. These results shed light on the complicated relationship between the polarity and magnitude of FACs and conductance at various MLTs. Several metrics (ME, RMSE, and PE) have been used to test the goodness of the estimations. For example, the RMSE of the Pedersen conductance specification is 3.17 mho, and the RMSE of the Hall conductance specification is 7.23 mho. These metrics indicate that the model can provide good estimates of the global conductance given the global FAC polarity and magnitude. A couple of limitations of the model have also been discussed: (1) the model may underestimate conductance during extreme events; (2) FACs are indirectly associated with the conductance; (3) the model needs to be further tested for other latitudes, such as the polar cap. Despite these limitations, this new model provides a convenient and accurate way to estimate the global conductance distributions in the high-latitude region and should be useful for high-latitude electrodynamics specification and space weather research.

Acknowledgments

ZW and SZ acknowledge 80NSSC21K0047, 80NSSC20K1313, and 80NSSC20K0190 for supporting this work. SWARM FAC data are available at <https://vires.services/>. PFISR data are available at <https://data.amisr.com/database>. Dst and F10.7 are available at <https://omniweb.gsfc.nasa.gov/>.

References

- Ahn, B.-H., Richmond, A. D., Kamide, Y., Kroehl, H. W., Emery, B. A., de la Beaujardière, O., & Akasofu, S.-I. (1998). An ionospheric conductance model based on ground magnetic disturbance data. *Journal of Geophysical Research: Space Physics*, 103(A7), 14769-14780. Retrieved from <https://agupubs.onlinelibrary.wiley.com/doi/abs/10.1029/97JA03088> doi: <https://doi.org/10.1029/97JA03088>
- Ahn, B.-H., Robinson, R., Kamide, Y., & Akasofu, S.-I. (1983). Electric conductivities, electric fields and auroral particle energy injection rate in the auroral ionosphere and their empirical relations to the horizontal magnetic disturbances. *Planetary and Space Science*, 31(6), 641-653. Retrieved from <https://www.sciencedirect.com/science/article/pii/0032063383900053> doi: [https://doi.org/10.1016/0032-0633\(83\)90005-3](https://doi.org/10.1016/0032-0633(83)90005-3)
- Anderson, B. J., Korth, H., Waters, C. L., Green, D. L., Merkin, V. G., Barnes, R. J., & Dyrud, L. P. (2014). Development of large-scale birkeland currents determined from the active magnetosphere and planetary electrodynamics response experiment. *Geophysical Research Letters*, 41(9), 3017-3025. Retrieved from <https://agupubs.onlinelibrary.wiley.com/doi/abs/10.1002/2014GL059941> doi: <https://doi.org/10.1002/2014GL059941>
- Carter, J. A., Milan, S. E., Coxon, J. C., Walach, M. T., & Anderson, B. J. (2016, 2). Average field-aligned current configuration parameterized by solar wind conditions. *Journal of Geophysical Research A: Space Physics*, 121, 1294-1307. doi: 10.1002/2015JA021567
- Carter, J. A., Milan, S. E., Paxton, L. J., Anderson, B. J., & Gjerloev, J. (2020).

- Height-integrated ionospheric conductances parameterized by interplanetary magnetic field and substorm phase. *Journal of Geophysical Research: Space Physics*, 125(10), e2020JA028121. Retrieved from <https://agupubs.onlinelibrary.wiley.com/doi/abs/10.1029/2020JA028121> (e2020JA028121 10.1029/2020JA028121) doi: <https://doi.org/10.1029/2020JA028121>
- Coumans, V., Gérard, J.-C., Hubert, B., Meurant, M., & Mende, S. B. (2004). Global auroral conductance distribution due to electron and proton precipitation from image-fuv observations. *Annales Geophysicae*, 22(5), 1595–1611. Retrieved from <https://angeo.copernicus.org/articles/22/1595/2004/> doi: 10.5194/angeo-22-1595-2004
- Fang, X., Lummerzheim, D., & Jackman, C. H. (2013). Proton impact ionization and a fast calculation method. *Journal of Geophysical Research: Space Physics*, 118(8), 5369–5378. Retrieved from <https://agupubs.onlinelibrary.wiley.com/doi/abs/10.1002/jgra.50484> doi: <https://doi.org/10.1002/jgra.50484>
- Fuller-Rowell, T., & Evans, D. (1987). Height-integrated pedersen and hall conductivity patterns inferred from the tiros-noaa satellite data. *Journal of Geophysical Research: Space Physics*, 92(A7), 7606–7618.
- Galand, M., & Richmond, A. D. (2001). Ionospheric electrical conductances produced by auroral proton precipitation. *Journal of Geophysical Research: Space Physics*, 106(A1), 117–125. Retrieved from <https://agupubs.onlinelibrary.wiley.com/doi/abs/10.1029/1999JA002001> doi: <https://doi.org/10.1029/1999JA002001>
- Germany, G., Torr, D., Richards, P., Torr, M., & John, S. (1994). Determination of ionospheric conductivities from fuv auroral emissions. *Journal of Geophysical Research: Space Physics*, 99(A12), 23297–23305.
- Gjerloev, J. W. (2012). The supermag data processing technique. *Journal of Geophysical Research: Space Physics*, 117(A9). Retrieved from <https://agupubs.onlinelibrary.wiley.com/doi/abs/10.1029/2012JA017683> doi: <https://doi.org/10.1029/2012JA017683>
- Grubbs II, G., Michell, R., Samara, M., Hampton, D., & Jahn, J.-M. (2018). Predicting electron population characteristics in 2-d using multispectral ground-based imaging. *Geophysical Research Letters*, 45(1), 15–20. Retrieved from <https://agupubs.onlinelibrary.wiley.com/doi/abs/10.1002/2017GL075873> doi: <https://doi.org/10.1002/2017GL075873>
- Hardy, D. A., Gussenhoven, M., Raistrick, R., & McNeil, W. (1987). Statistical and functional representations of the pattern of auroral energy flux, number flux, and conductivity. *Journal of Geophysical Research: Space Physics*, 92(A11), 12275–12294.
- He, M., Vogt, J., Lühr, H., Sorbalo, E., Blagau, A., Le, G., & Lu, G. (2012). A high-resolution model of field-aligned currents through empirical orthogonal functions analysis (mface). *Geophysical Research Letters*, 39(18). doi: <https://doi.org/10.1029/2012GL053168>
- Heinselman, C. J., & Nicolls, M. J. (2008). A bayesian approach to electric field and e-region neutral wind estimation with the poker flat advanced modular incoherent scatter radar. *Radio Science*, 43(5).
- Iijima, T., & Potemra, T. A. (1978). Large-scale characteristics of field-aligned currents associated with substorms. *Journal of Geophysical Research: Space Physics*, 83(A2), 599–615.
- Kaeppler, S. R., Hampton, D. L., Nicolls, M. J., Strømme, A., Solomon, S. C., Hecht, J. H., & Conde, M. G. (2015). An investigation comparing ground-based techniques that quantify auroral electron flux and conductance. *Journal of Geophysical Research A: Space Physics*, 120(10), 9038–9056. doi: 10.1002/2015JA021396

- 495 Kamide, Y. (1982). The relationship between field-aligned currents and the auroral
496 electrojets: A review. *Space Science Reviews*, 31(2), 127–243. Retrieved 2021-
497 10-11, from <http://link.springer.com/10.1007/BF00215281> doi: 10.1007/
498 BF00215281
- 499 Karlsson, T., Brenning, N., Marghitu, O., Marklund, G., & Buchert, S. (2007).
500 High-altitude signatures of ionospheric density depletions caused by field-
501 aligned currents. *arXiv preprint arXiv:0704.1610*.
- 502 Karlsson, T., & Marklund, G. (1998). Simulations of effects of small-scale auro-
503 ral current closure in the return current region. *Physics of space plasmas*, 15,
504 401.
- 505 Knight, S. (1973). Parallel electric fields. *Planetary and Space Science*, 21(5), 741–
506 750.
- 507 Korth, H., Zhang, Y., Anderson, B. J., Sotirelis, T., & Waters, C. L. (2014). Statis-
508 tical relationship between large-scale upward field-aligned currents and electron
509 precipitation. *Journal of Geophysical Research: Space Physics*, 119(8), 6715-
510 6731. Retrieved from [https://agupubs.onlinelibrary.wiley.com/doi/abs/](https://agupubs.onlinelibrary.wiley.com/doi/abs/10.1002/2014JA019961)
511 [10.1002/2014JA019961](https://doi.org/10.1002/2014JA019961) doi: <https://doi.org/10.1002/2014JA019961>
- 512 Lühr, H., Huang, T., Wing, S., Kervalishvili, G., Rauberg, J., & Korth, H. (2016).
513 Filamentary field-aligned currents at the polar cap region during northward in-
514 terplanetary magnetic field derived with the swarm constellation. *Annales Geo-*
515 *physicae*, 34(10), 901–915. Retrieved from [https://angeo.copernicus.org/](https://angeo.copernicus.org/articles/34/901/2016/)
516 [articles/34/901/2016/](https://doi.org/10.5194/angeo-34-901-2016) doi: 10.5194/angeo-34-901-2016
- 517 Lühr, H., Park, J., Gjerloev, J. W., Rauberg, J., Michaelis, I., Merayo, J. M. G.,
518 & Brauer, P. (2014). Field-aligned currents’ scale analysis performed with
519 the Swarm constellation Special Section :. *Geophys. Res. Lett.*, 1–8. doi:
520 10.1002/2014GL062453.We
- 521 Lummerzheim, D., Rees, M. H., Craven, J. D., & Frank, L. A. (1991). Ionospheric
522 conductances derived from DE-1 auroral images. *J. Atmos. Terr. Phys.*.
- 523 McGranaghan, R., Knipp, D. J., Matsuo, T., Godinez, H., Redmon, R. J., Solomon,
524 S. C., & Morley, S. K. (2015). Modes of high-latitude auroral conductance
525 variability derived from dmsp energetic electron precipitation observations:
526 Empirical orthogonal function analysis. *Journal of Geophysical Research:*
527 *Space Physics*, 120(12), 11–013.
- 528 Moen, J., & Brekke, A. (1993). The solar flux influence on quiet time conductances
529 in the auroral ionosphere. *Geophysical Research Letters*, 20(10), 971–974. doi:
530 10.1029/92GL02109
- 531 Mukhopadhyay, A., Welling, D. T., Liemohn, M. W., Ridley, A. J., Chakraborty, S.,
532 & Anderson, B. J. (2020). Conductance Model for Extreme Events: Impact of
533 Auroral Conductance on Space Weather Forecasts. *Space Weather*, 1–27. doi:
534 10.1029/2020sw002551
- 535 Murphy, K. R., Mann, I. R., Rae, I. J., Waters, C. L., Frey, H. U., Kale, A., ...
536 Korth, H. (2013). The detailed spatial structure of field-aligned cur-
537 rents comprising the substorm current wedge. *Journal of Geophysical*
538 *Research: Space Physics*, 118(12), 7714-7727. Retrieved from [https://](https://agupubs.onlinelibrary.wiley.com/doi/abs/10.1002/2013JA018979)
539 [agupubs.onlinelibrary.wiley.com/doi/abs/10.1002/2013JA018979](https://doi.org/10.1002/2013JA018979) doi:
540 <https://doi.org/10.1002/2013JA018979>
- 541 Newell, P. T., Sotirelis, T., & Wing, S. (2009, 9). Diffuse, monoenergetic,
542 and broadband aurora: The global precipitation budget. *Journal of Geo-*
543 *physical Research: Space Physics*, 114, 9207. Retrieved from [https://](https://agupubs.onlinelibrary.wiley.com/doi/full/10.1029/2009JA014326)
544 [agupubs.onlinelibrary.wiley.com/doi/full/10.1029/2009JA014326](https://doi.org/10.1029/2009JA014326)
545 doi: 10.1029/2009JA014326
- 546 Newell, P. T., Sotirelis, T., & Wing, S. (2010). Seasonal variations in diffuse, mo-
547 noenergetic, and broadband aurora. *Journal of Geophysical Research: Space*
548 *Physics*, 115(A3).
- 549 Picone, J. M., Hedin, A. E., Drob, D. P., & Aikin, A. C. (2002). Nrlmsise-00 em-

- pirical model of the atmosphere: Statistical comparisons and scientific issues. *Journal of Geophysical Research: Space Physics*, 107(A12), SIA 15-1-SIA 15-16. Retrieved from <https://agupubs.onlinelibrary.wiley.com/doi/abs/10.1029/2002JA009430> doi: <https://doi.org/10.1029/2002JA009430>
- Pulkkinen, A., Rastätter, L., Kuznetsova, M., Singer, H., Balch, C., Weimer, D., ... Weigel, R. (2013). Community-wide validation of geospace model ground magnetic field perturbation predictions to support model transition to operations. *Space Weather*, 11(6), 369-385. Retrieved from <https://agupubs.onlinelibrary.wiley.com/doi/abs/10.1002/swe.20056> doi: <https://doi.org/10.1002/swe.20056>
- Ridley, A. J., Gombosi, T. I., Dezeew, D. L., Ridley, A. J., Gombosi, T. I., Ionospheric, D. L. D., ... Dezeew, D. L. (2004). Ionospheric control of the magnetosphere : conductance. *Annales Geophysicae*, 22(2), 567-584.
- Ritter, P., Lühr, H., & Rauberg, J. (2013). Determining field-aligned currents with the swarm constellation mission. *Earth, Planets and Space*, 65(11), 1285-1294.
- Robinson, R. M., Kaeppler, S. R., Zanetti, L., Anderson, B., Vines, S. K., Korth, H., & Fitzmaurice, A. (2020). Statistical relations between auroral electrical conductances and field-aligned currents at high latitudes. *Journal of Geophysical Research: Space Physics*, 1-16. doi: 10.1029/2020ja028008
- Robinson, R. M., Vondrak, R. R., Miller, K., Dabbs, T., & Hardy, D. (1987). On calculating ionospheric conductances from the flux and energy of precipitating electrons. *Journal of Geophysical Research*, 92(A3), 2565. Retrieved from <http://doi.wiley.com/10.1029/JA092iA03p02565> doi: 10.1029/JA092iA03p02565
- Robinson, R. M., Zanetti, L., Anderson, B., Vines, S., & Gjerloev, J. (2021). Determination of auroral electrodynamic parameters from ampere field-aligned current measurements. *Space Weather*, 19(4), e2020SW002677. Retrieved from <https://agupubs.onlinelibrary.wiley.com/doi/abs/10.1029/2020SW002677> (e2020SW002677 2020SW002677) doi: <https://doi.org/10.1029/2020SW002677>
- Robinson, R. M., & Zanetti, L. J. (2021). Auroral energy flux and joule heating derived from global maps of field-aligned currents. *Geophysical Research Letters*, 48(7), e2020GL091527. Retrieved from <https://agupubs.onlinelibrary.wiley.com/doi/abs/10.1029/2020GL091527> (e2020GL091527 2020GL091527) doi: <https://doi.org/10.1029/2020GL091527>
- Robinson, R. M., Zhang, Y., Anderson, B. J., Zanetti, L. J., Korth, H., & Fitzmaurice, A. (2018). Statistical Relations Between Field-Aligned Currents and Precipitating Electron Energy Flux. *Geophysical Research Letters*, 45(17), 8738-8745. doi: 10.1029/2018GL078718
- Schunk, R., & Nagy, A. (2009). *Ionospheres: physics, plasma physics, and chemistry*. Cambridge university press.
- Shepherd, S. (2014). Altitude-adjusted corrected geomagnetic coordinates: Definition and functional approximations. *Journal of Geophysical Research: Space Physics*, 119(9), 7501-7521.
- Solomon, S. C., Hays, P. B., & Abreu, V. J. (1988). The auroral 6300 Å emission: Observations and modeling. *Journal of Geophysical Research: Space Physics*, 93(A9), 9867-9882.
- Spiro, R., Reiff, P. H., & Maher Jr, L. (1982). Precipitating electron energy flux and auroral zone conductances-an empirical model. *Journal of Geophysical Research: Space Physics*, 87(A10), 8215-8227.
- Thébault, E., Finlay, C. C., Beggan, C. D., Alken, P., Aubert, J., Barrois, O., ... others (2015). International geomagnetic reference field: the 12th generation. *Earth, Planets and Space*, 67(1), 1-19.
- Wallis, D. D., & Budzinski, E. E. (1981, 1). Empirical models of height integrated

- conductivities. *Journal of Geophysical Research: Space Physics*, 86, 125-137.
Retrieved from <https://agupubs.pericles-prod.literatumonline.com/doi/full/10.1029/JA086iA01p00125>
<https://agupubs.pericles-prod.literatumonline.com/doi/abs/10.1029/JA086iA01p00125>
<https://agupubs.onlinelibrary.wiley.com/doi/10.1029/JA086iA01p00125> doi: 10.1029/JA086iA01p00125
- Weygand, J. M., Amm, O., Viljanen, A., Angelopoulos, V., Murr, D., Engebretson, M. J., ... Mann, I. (2011, 3). Application and validation of the spherical elementary currents systems technique for deriving ionospheric equivalent currents with the north american and greenland ground magnetometer arrays. *Journal of Geophysical Research: Space Physics*, 116. Retrieved from <https://agupubs.onlinelibrary.wiley.com/doi/full/10.1029/2010JA016177>
<https://agupubs.onlinelibrary.wiley.com/doi/abs/10.1029/2010JA016177>
<https://agupubs.onlinelibrary.wiley.com/doi/10.1029/2010JA016177> doi: 10.1029/2010JA016177
- Xiong, C., Stolle, C., Alken, P., & Rauberg, J. (2020, 10). Relationship between large-scale ionospheric field-aligned currents and electron/ion precipitations: Dmsp observations. *Earth, Planets and Space* 72:1, 72, 1-22. Retrieved from <https://earth-planets-space.springeropen.com/articles/10.1186/s40623-020-01286-z> doi: 10.1186/S40623-020-01286-Z
- Zou, S., Lyons, L., Nicolls, M., Heinselman, C., & Mende, S. (2009). Nightside ionospheric electrodynamics associated with substorms: PFISR and THEMIS ASI observations. *Journal of Geophysical Research: Space Physics*, 114 (A12).
- Zou, S., Moldwin, M. B., Nicolls, M. J., Ridley, A. J., Coster, A. J., Yizengaw, E., ... Donovan, E. F. (2013). Electrodynamics of the high-latitude trough: Its relationship with convection flows and field-aligned currents. *Journal of Geophysical Research: Space Physics*, 118(5), 2565–2572.

Table 1. Fitting Parameters

MLT	k_{UvsP}	b_{UvsP}	k_{UvsH}	b_{UvsH}	k_{DvsP}	b_{DvsP}	k_{DvsH}	b_{DvsH}
0-3	0.287	2.47	0.345	3.14	0.155	2.26	0.178	2.78
3-6	0.365	2.55	0.439	3.41	0.217	2.17	0.276	2.99
6-9	0.133	1.67	0.266	2.83	-0.01689 (0)	0.996	0.105	2.00
9-12	0.0665*	1.38*	0.136*	2.11*	0.0141*	1.16*	0.0638*	1.81*
12-15	-0.0134 (0)	1.08	0.00592	1.38	0.0281	1.33	0.0226	1.62
15-18	0.0827	1.38	0.0634	1.63	0.132	1.63	0.109	1.91
18-21	0.196	2.15	0.177	2.37	0.138	1.75	0.142	2.11
21-0	0.274	2.36	0.303	2.86	0.203	2.05	0.214	2.46

* means that the values are calculated by interpolation. (0) means that the negative values are replaced with 0 in the application.

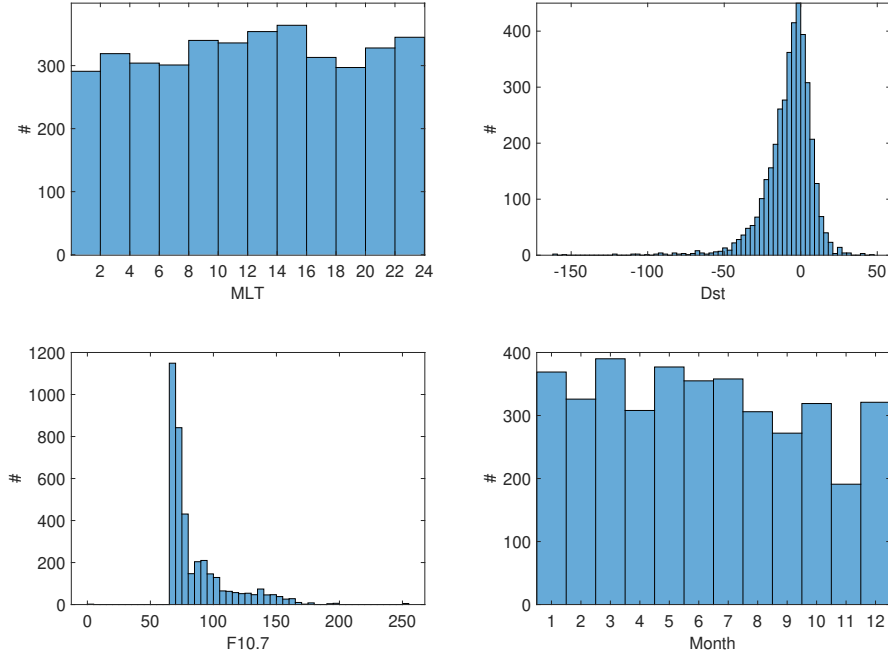


Figure 1. Distributions of MLT, Dst, F10.7, and month in the whole dataset.

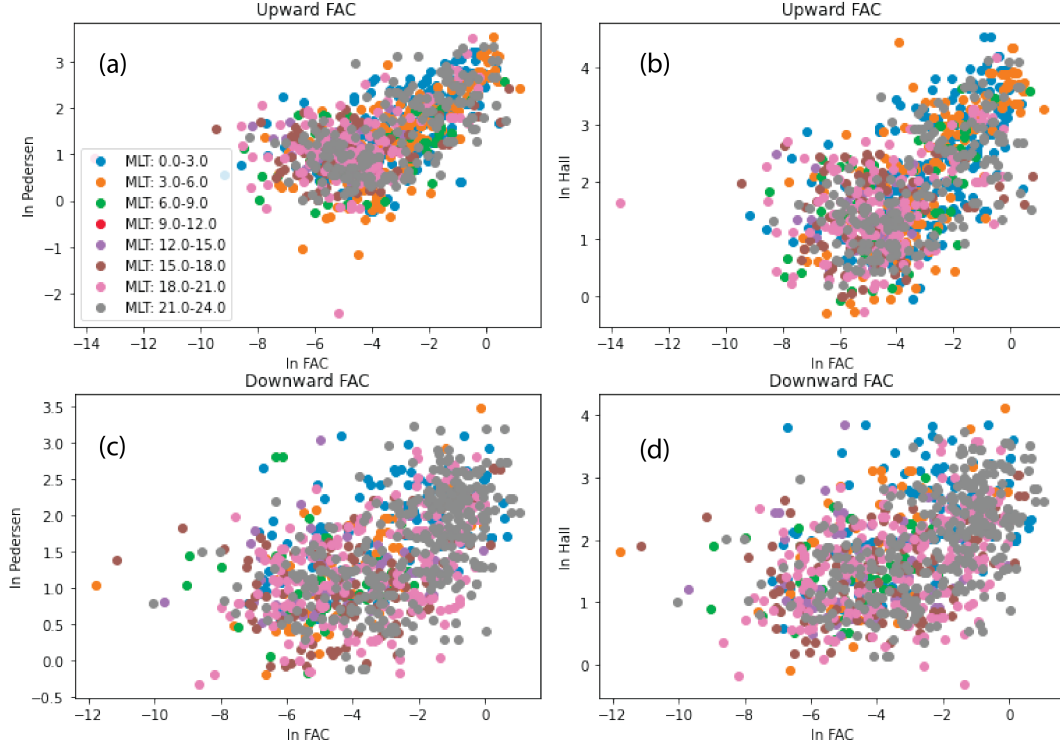


Figure 2. The scattering plots of the FACs and conductance in a log-log scale. The unit of the FACs is $\mu A/m^2$, and the unit of conductance is mho. The colors represent MLTs. (a) Upward FAC vs Pedersen conductance. (b) Upward FAC vs Hall conductance. (c) Downward FAC vs Pedersen conductance. (d) Downward FAC vs Hall conductance.

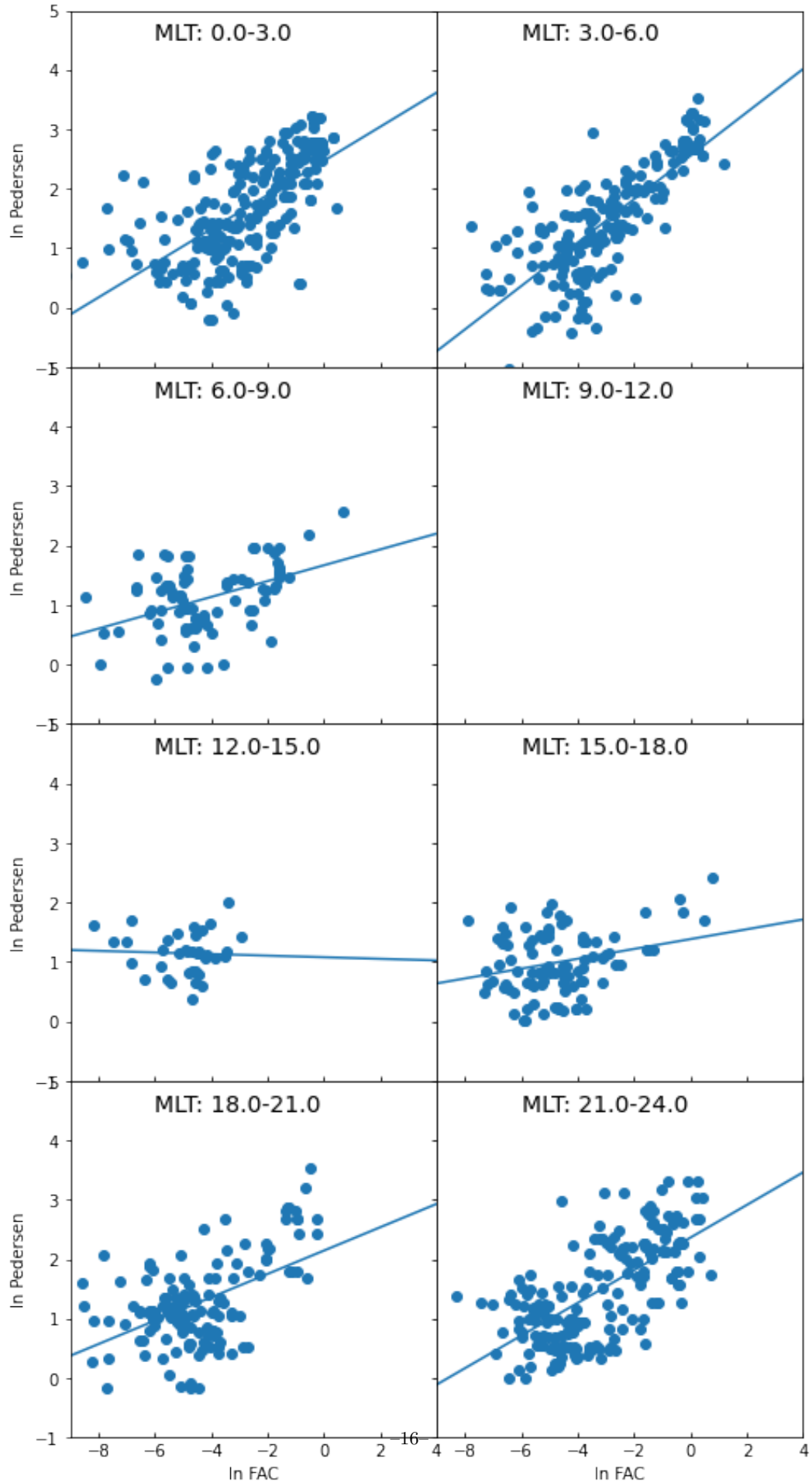


Figure 3. Statistical relations between Pedersen conductance and upward FACs in a log-log scale at different MLTs.

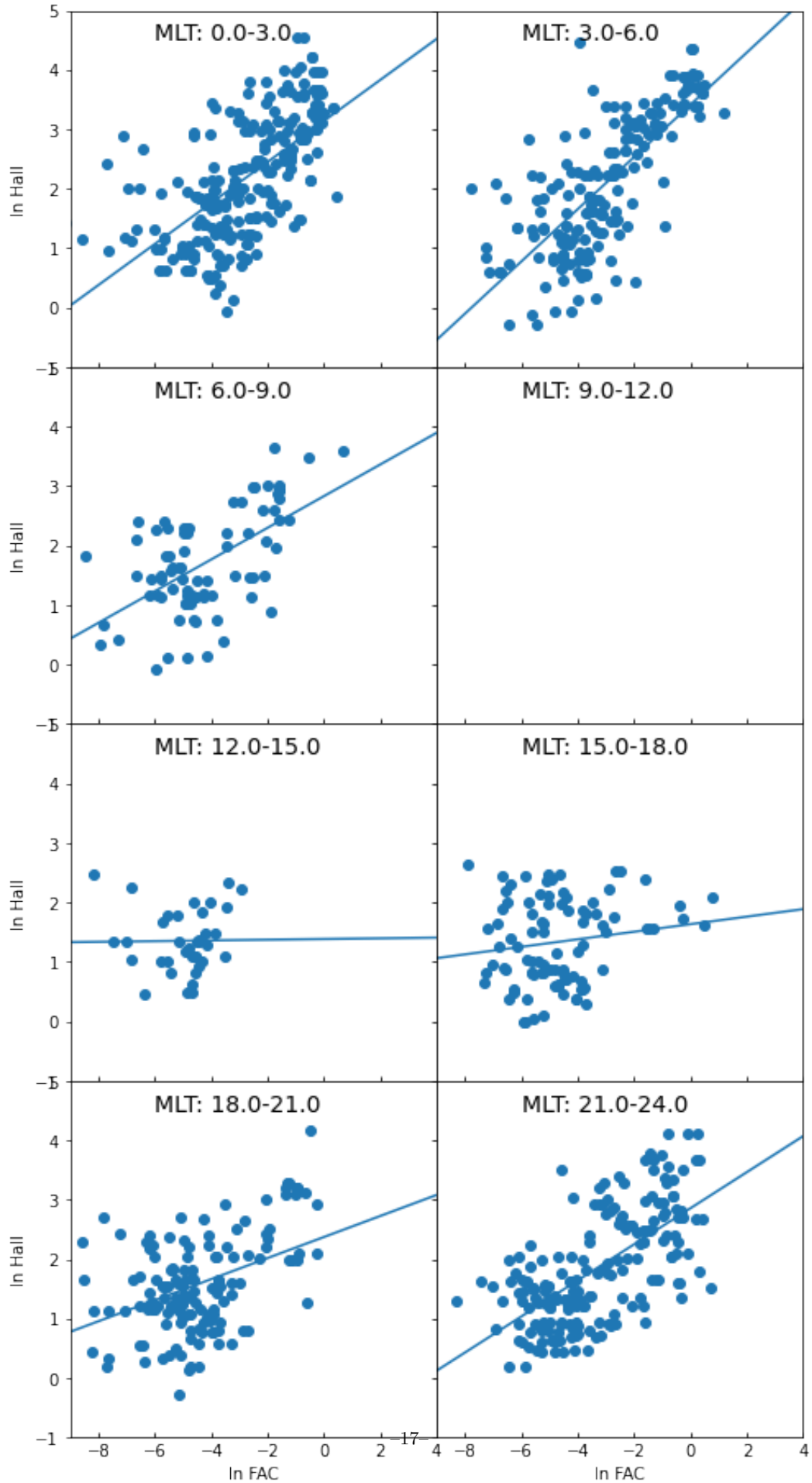


Figure 4. Statistical relations between Hall conductance and upward FACs in a log-log scale at different MLTs.

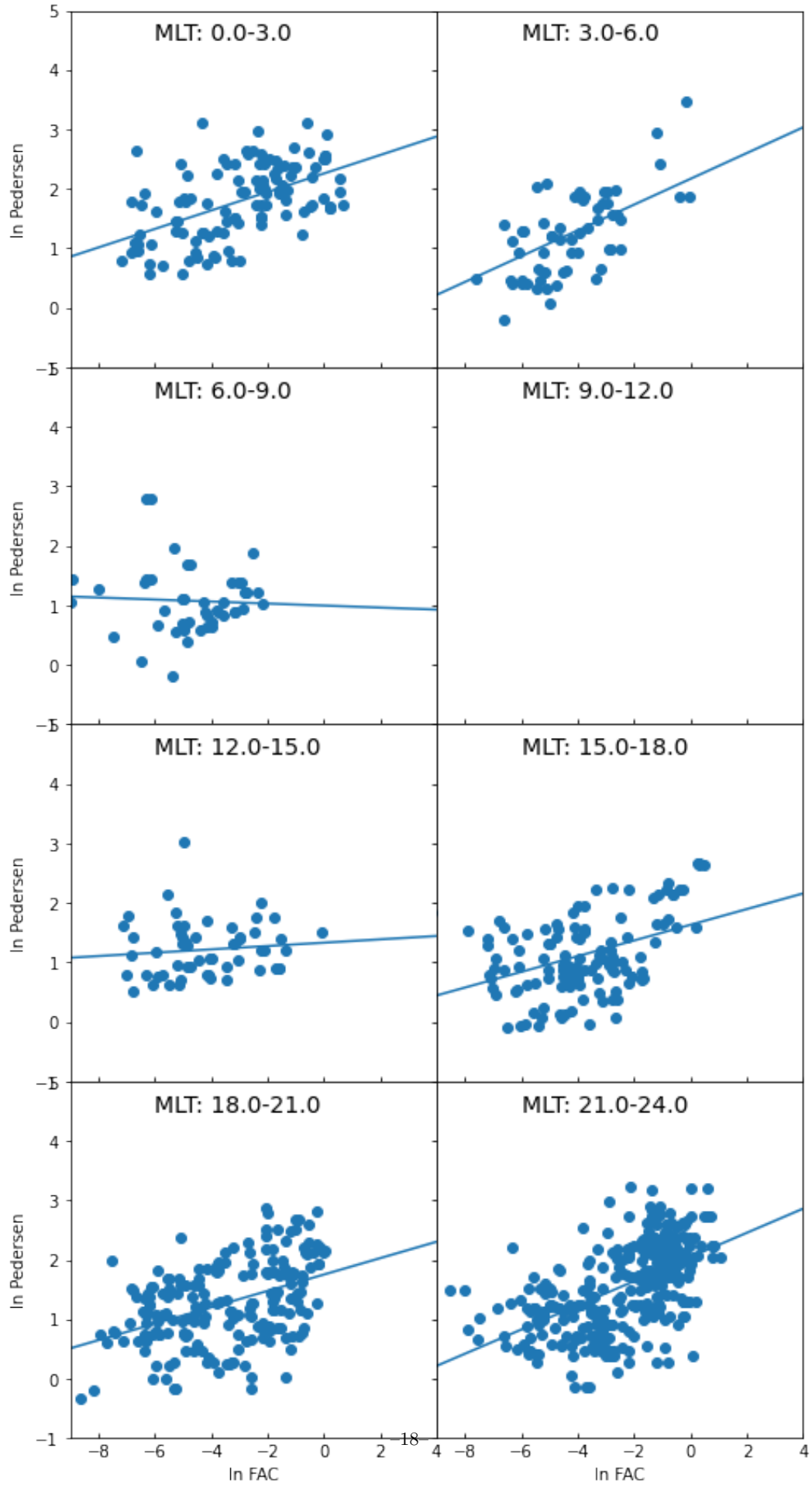


Figure 5. Statistical relations between Pedersen conductance and downward FACs in a log-log scale at different MLTs.

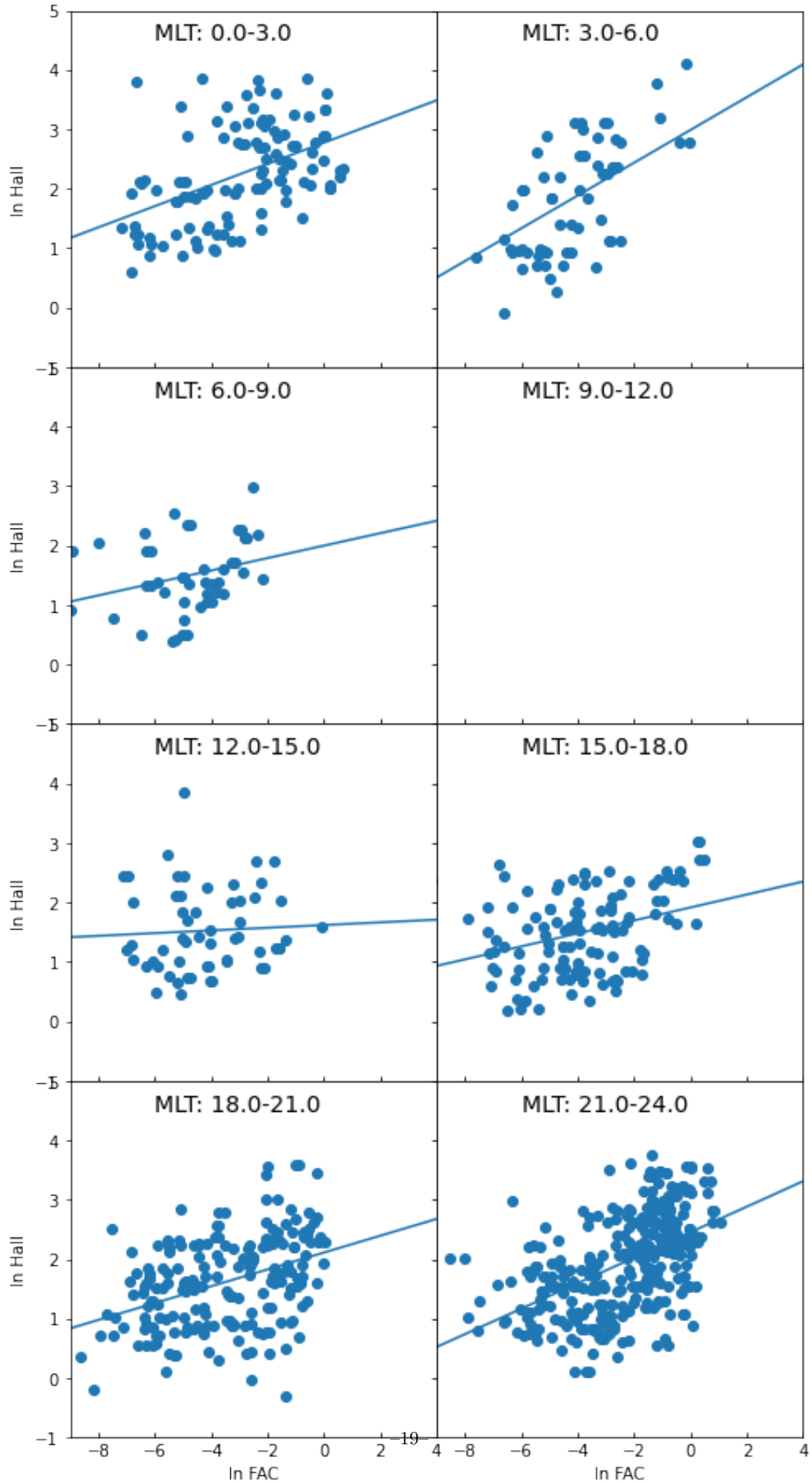


Figure 6. Statistical relations between Hall conductance and downward FACs in a log-log scale at different MLTs.

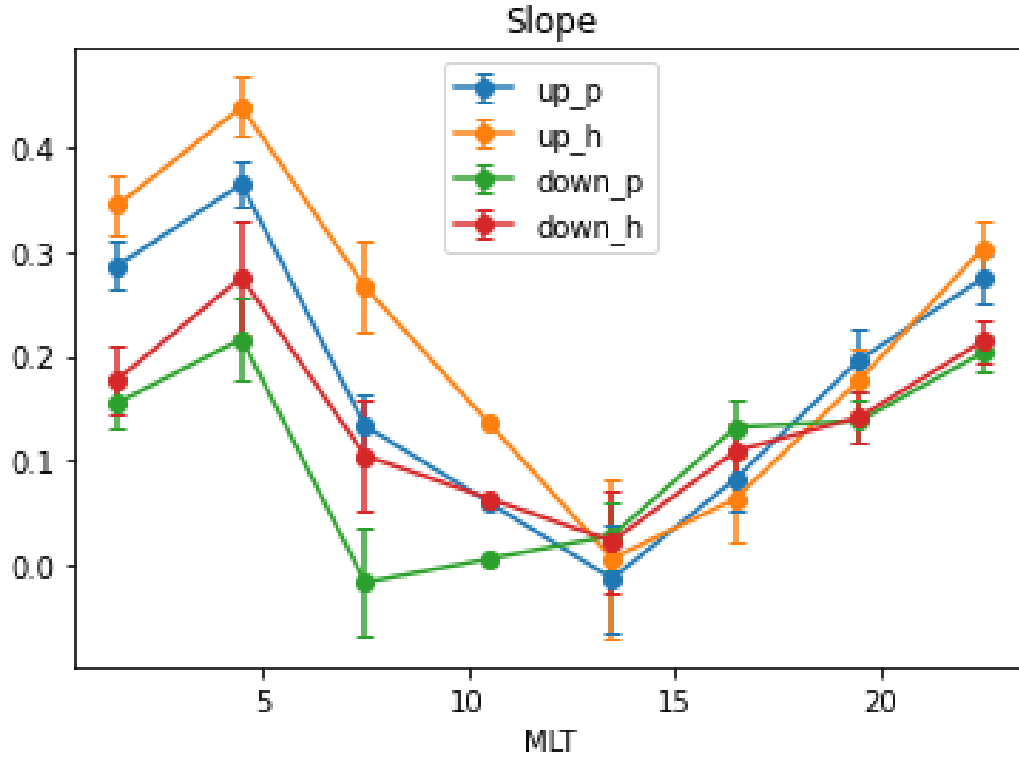


Figure 7. The dependence of slopes on MLTs.

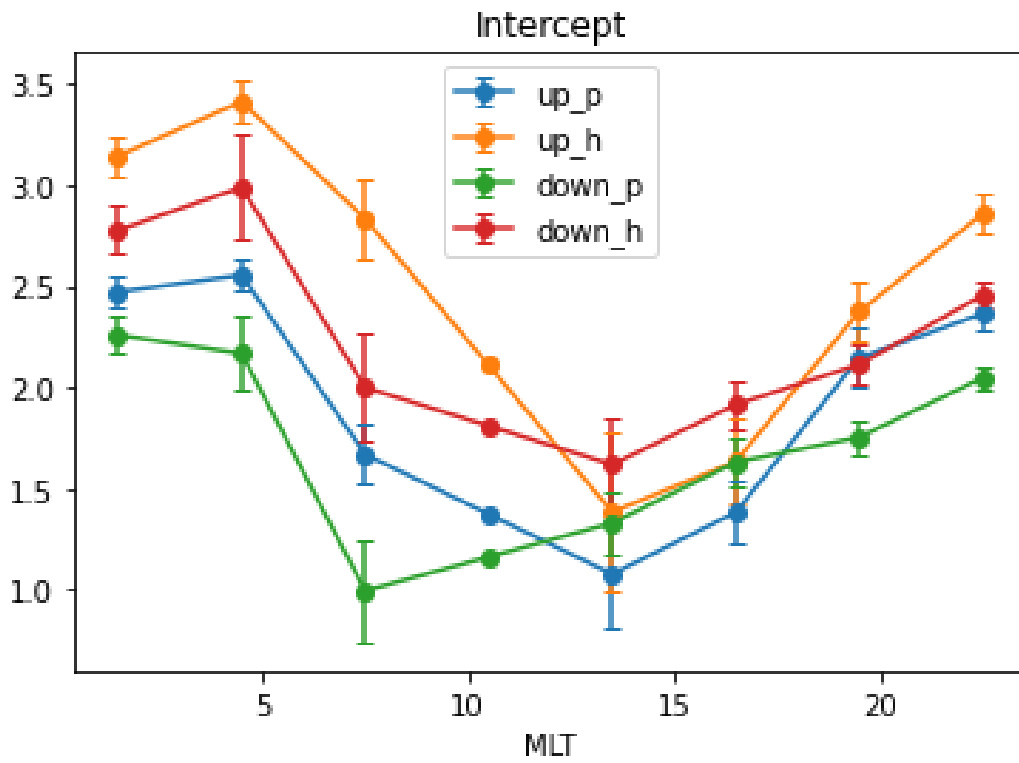


Figure 8. The dependence of intercepts on MLTs.

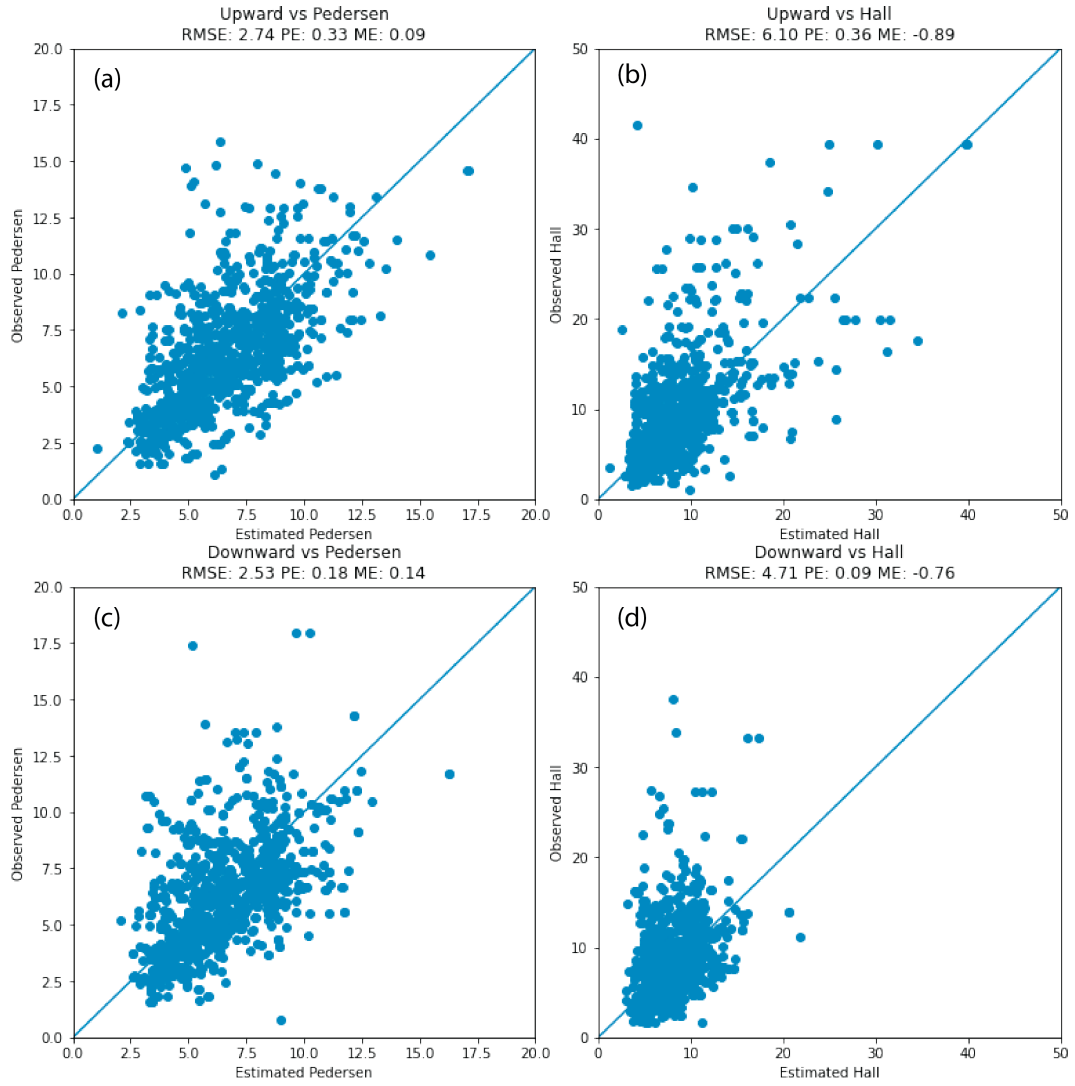


Figure 9. Comparisons between the estimated conductance and the observed conductance. RMSE, PE, ME are printed in the title of each panel.

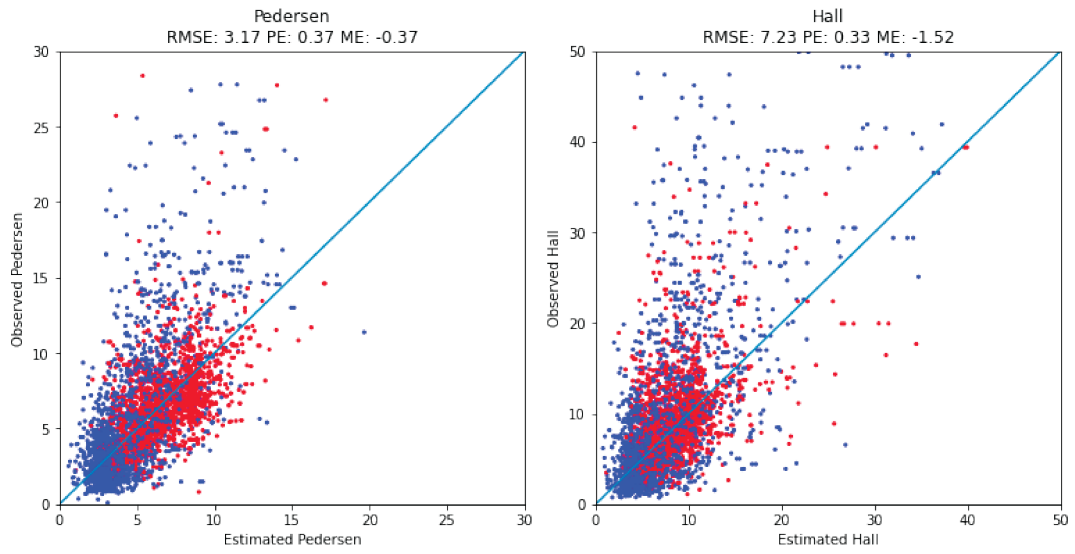


Figure 10. Comparisons between the estimated conductance and the observed conductance in the whole dataset. Red points represent in sunlight, while blue points represent in darkness. RMSE, PE, ME are printed in the title of each panel.